Supporting Information for

Nanoscale thermal transport at PbTe grain boundaries: a neural-network-potential molecular dynamics study

Susumu Fujii,[1, 2, *] Tatsuya Yokoi,[3, †] and Katsuyuki Matsunaga[2, 3]
[1] *Department of Materials, Kyushu University, Fukuoka 819-0377, Japan*
[2] *Nanostructures Research Laboratory, Japan Fine Ceramics Center, Nagoya, 456-8587, Japan*
[3] *Department of Materials Physics, Nagoya University, Nagoya 464-8603, Japan*
(Dated: February 12, 2026)

S1. Training dataset

As summarized in Table S1, the training dataset included not only pristine systems but also native point defects, surfaces and grain boundaries (GBs) in order to cover a wide range of atomic configurations. The dataset for the bulk lattice is the same as that used in our previous study [1] and was constructed from 1 × 1 × 1, 2 × 1 × 1, 2 × 2 × 2 and 3 × 3 × 3 supercells of the conventional unit cell. These reference structures contained Pb/Te vacancies, antisites or interstitials, assuming that their charge states were neutral. These point defects were introduced by varying their number and formation sites. For surfaces, several lattice planes with low Miller indices were considered: (001), (110), (111), (112) and (310). For GBs, seven symmetric tilt GBs (STGBs) with the [001] or $[1\bar{1}0]$ rotation axes were considered. Our previous studies indicated that including several STGBs in the training dataset improves the predictive accuracy of neural-network potentials (NNPs) even for GBs that are not included in the training dataset [2–4]. In addition, a (001)/(110) incoherent asymmetric tilt GB (ATGB) was also considered to facilitate the future application of the NNP to crystallographically diverse GBs, although the present study focuses only on symmetric tilt GBs.

TABLE S1. Training dataset for the NNP.

Reference structure		Number of atoms	Amount of data		
			Energy	Force	Stress
Single crystal	1 × 1 × 1 cell	8	5,500	132,000	33,000
	2 × 1 × 1 cell	14-16	5,090	233,112	30,540
	2 × 2 × 2 cell	60-65	14,057	2,679,606	84,342
	3 × 3 × 3 cell	212-216	500	322,740	3,000
Surface	(100) plane	16	1,000	48,000	6,000
	(110) plane	16	1,000	48,000	6,000
	(310) plane	20	1,000	60,000	6,000
	(111) plane	12	1,000	36,000	6,000
	(112) plane	24	1,000	72,000	6,000
Grain boundary	$\Sigma5(210)/[001]$ STGB	36-40	3,000	348,984	18,000
	$\Sigma5(310)/[001]$ STGB	40	3,000	360,000	18,000
	$\Sigma3(111)/[1\bar{1}0]$ STGB	24	3,000	216,000	18,000
	$\Sigma3(112)/[1\bar{1}0]$ STGB	48	3,000	432,000	18,000
	$\Sigma9(221)/[1\bar{1}0]$ STGB	36	3,000	324,000	18,000
	$\Sigma9(114)/[1\bar{1}0]$ STGB	40	3,000	360,000	18,000
	$\Sigma11(113)/[1\bar{1}0]$ STGB	42-44	2,996	394,476	17,976
	(100)/(110) ATGB	66-68	1,926	391,566	11,556
	Total		53,069	6,458,484	318,414

---

[*] fujii.susumu.878@m.kyushu-u.ac.jp

[†] yokoi@mp.pse.nagoya-u.ac.jp

S2. Predictive accuracy

TABLE S2. Mean absolute errors (MAEs) of atomic forces in MD simulations.

Grain boundary	MAE (meV/Å)		
	200 (K)	400 (K)	600 (K)
$\Sigma5(210)/[001]$	27.6	35.7	45.5
$\Sigma5(310)/[001]$	28.4	35.6	41.8
$\Sigma13(320)/[001]$	33.3	38.6	44.0
$\Sigma13(510)/[001]$	31.0	37.6	45.7
$\Sigma17(410)/[001]$	31.1	38.5	46.6
$\Sigma17(530)/[001]$	33.4	40.2	46.4
$\Sigma3(111)/[1\bar{1}0]$	27.2	34.8	41.8
$\Sigma3(112)/[1\bar{1}0]$	31.3	45.4	56.3
$\Sigma9(221)/[1\bar{1}0]$	41.9	44.5	51.8
$\Sigma9(114)/[1\bar{1}0]$	36.2	42.0	47.7
$\Sigma11(332)/[1\bar{1}0]$	49.1	52.5	54.9
$\Sigma11(113)/[1\bar{1}0]$	36.2	45.5	53.0
$\Sigma17(223)/[1\bar{1}0]$	49.3	54.8	60.4
$\Sigma17(334)/[1\bar{1}0]$	46.8	51.5	55.2

S3. Detailed procedure for calculating thermal conductivity

First, molecular dynamics (MD) simulations were performed in the NPT ensemble at a temperature of 300 K and a pressure of 1 atm with a timestep of 5 fs and a total of 100,000 steps (0.5 ns). Velocity scaling was applied during the initial 0.1 ns to accelerate the system toward thermal equilibrium, followed by the Nosé-Hoover thermostat for the subsequent 0.4 ns. The equilibrium lattice constant at 300 K was determined from the cell lengths averaged over the final 0.1 ns of the NPT run. Next, NVT-MD simulations were performed for 2 ns (400,000 steps) using the fixed lattice constant obtained above. Velocity scaling was applied during the initial 0.5 ns, and the Nosé-Hoover thermostat was used for the remaining 1.5 ns. Subsequently, Perturbed MD (PMD) simulations were carried out for 15.5 ns (3,100,000 steps) along each of the x, y, and z directions using the Nosé-Hoover thermostat. The κ_{l} and $\kappa_{\mathrm{l},i}^{\mathrm{atom}}$ were evaluated from the time-averaged heat flux over the final 15 ns. To improve the statistical accuracy, five independent PMD simulations with different perturbations ($F_{\mathrm{ext}} = 2.6$–3.0×10^{-4} Å^{-1}) were conducted for each direction, and the average and standard error of κ_{l} were obtained. For $\kappa_{\mathrm{l},i}^{\mathrm{atom}}$, the symmetry of the GB models was analyzed using spglib [5], and the average and standard error of $\kappa_{\mathrm{l},i}^{\mathrm{atom}}$ were calculated for symmetrically equivalent atomic sites. Because the spectral κ_{l} converges slowly, it was evaluated from separate perturbed MD simulations with a longer simulation time 55 ns (11,000,000 steps). The harmonic phonon frequencies and eigenvectors necessary for modal decomposition were obtained using the Phonopy code [6, 7].

S4. GB structure

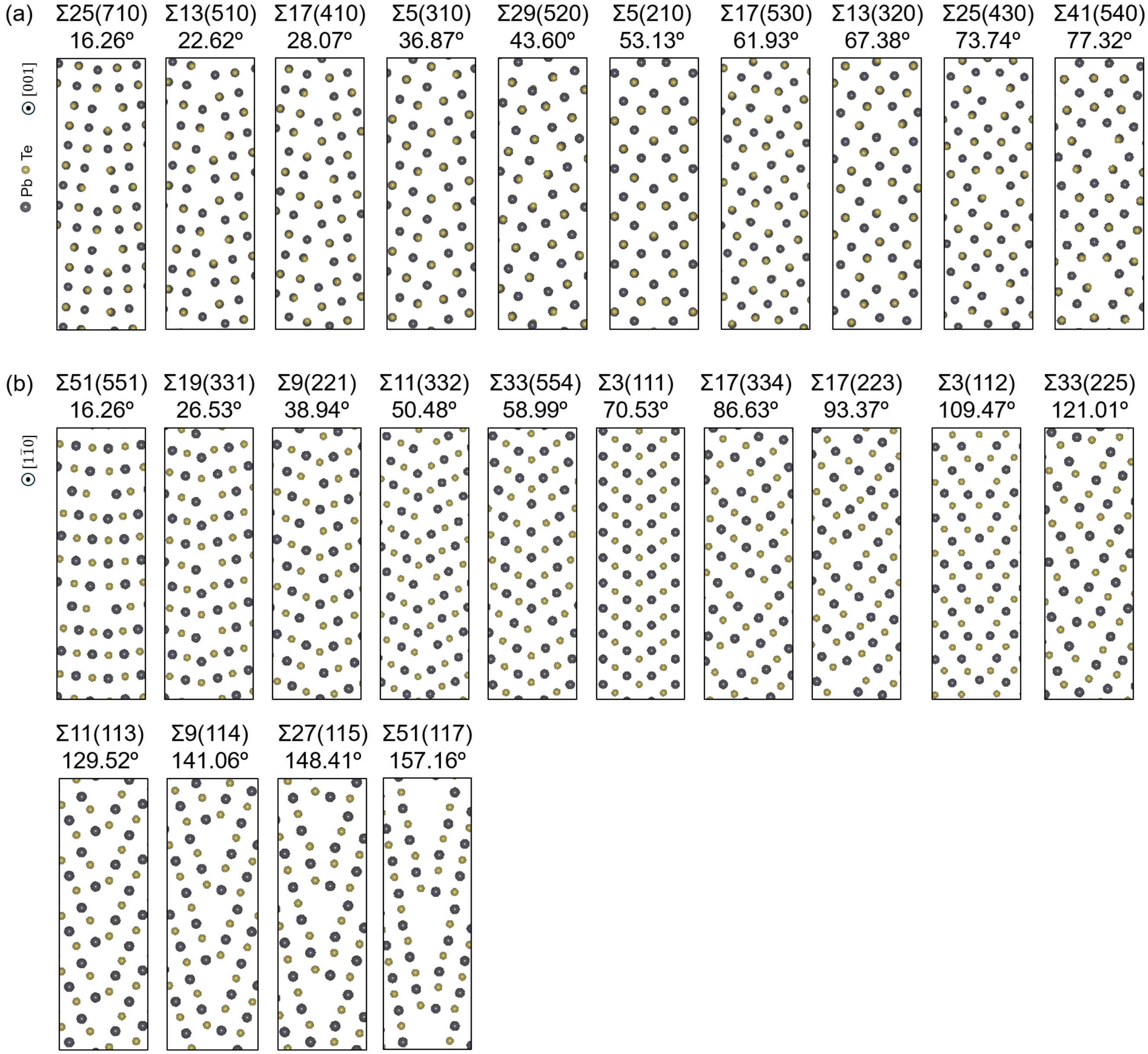

FIG. S1. Atomic structures of symmetric tilt GBs at 0 K for (a) the [001] system and (b) the [1$\bar{1}$0] system.

S5. Lattice thermal conductivity

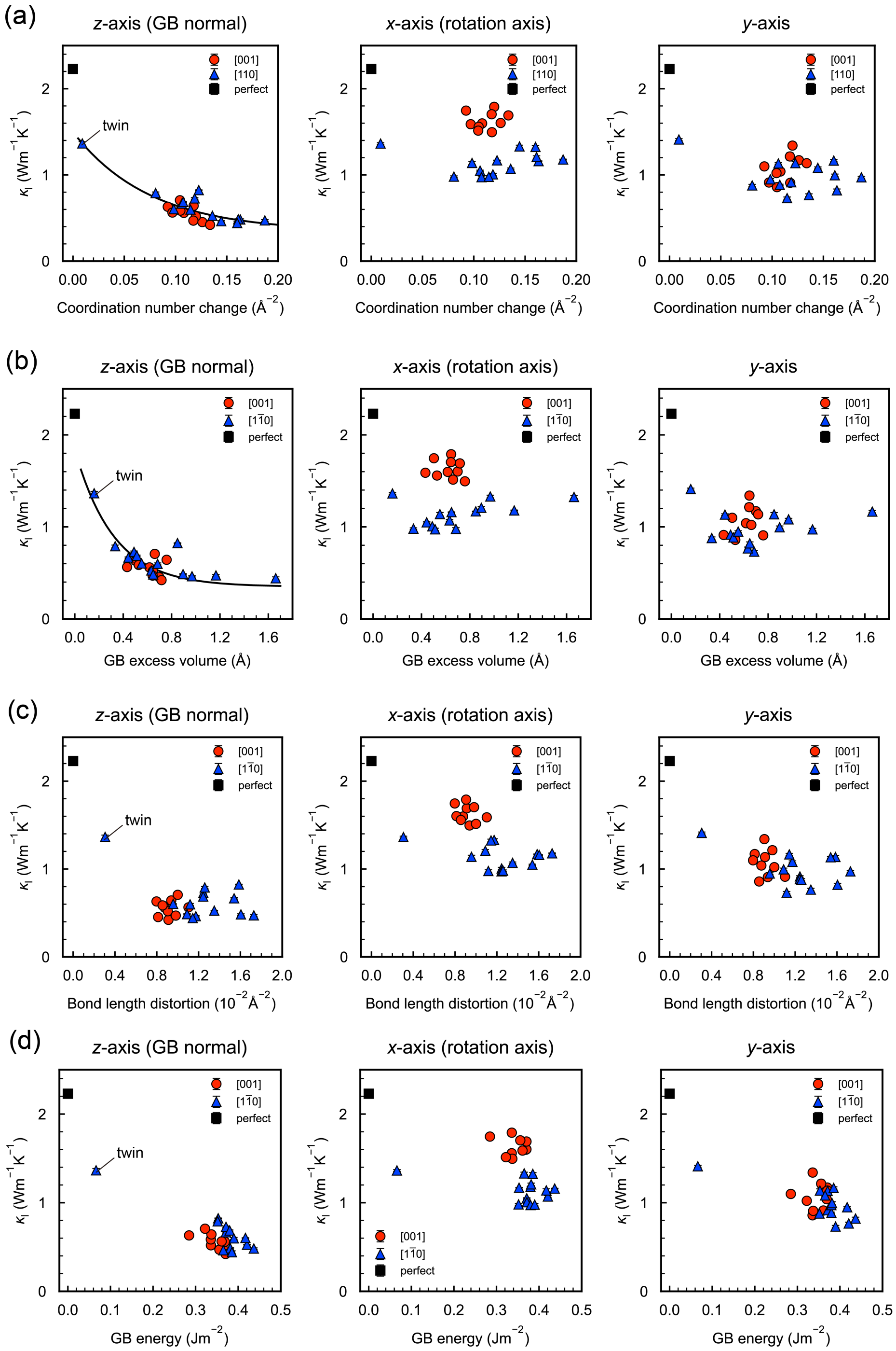

FIG. S2. Lattice thermal conductivity κ_l at 300 K as a function of (a) coordination-number change and (b) GB excess volume, (c) bond-length distortion, and (d) GB energy for the three axial directions, obtained from the lowest-energy structures optimized at 0 K. The correlation becomes weak particularly along the directions parallel to the GB planes ($x-$ and y-axes).

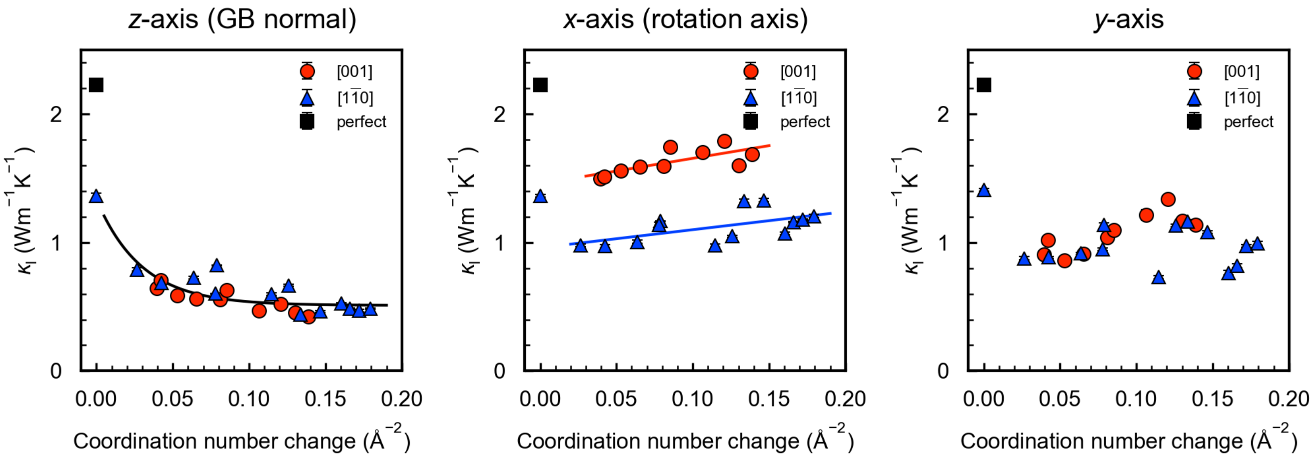

FIG. S3. Lattice thermal conductivity κ_l as a function of coordination-number change. The coordination number is defined as the number of atoms within a uniform cutoff distance between the first- and second-nearest-neighbor shells. When such an integer-valued coordination number is used instead of the continuous (Fermi-smeared) definition adopted in the main text, the twin GB becomes indistinguishable from the perfect crystal, and the difference between the twin and other GBs is reduced. Nevertheless, the overall trend remains the same for both definitions.

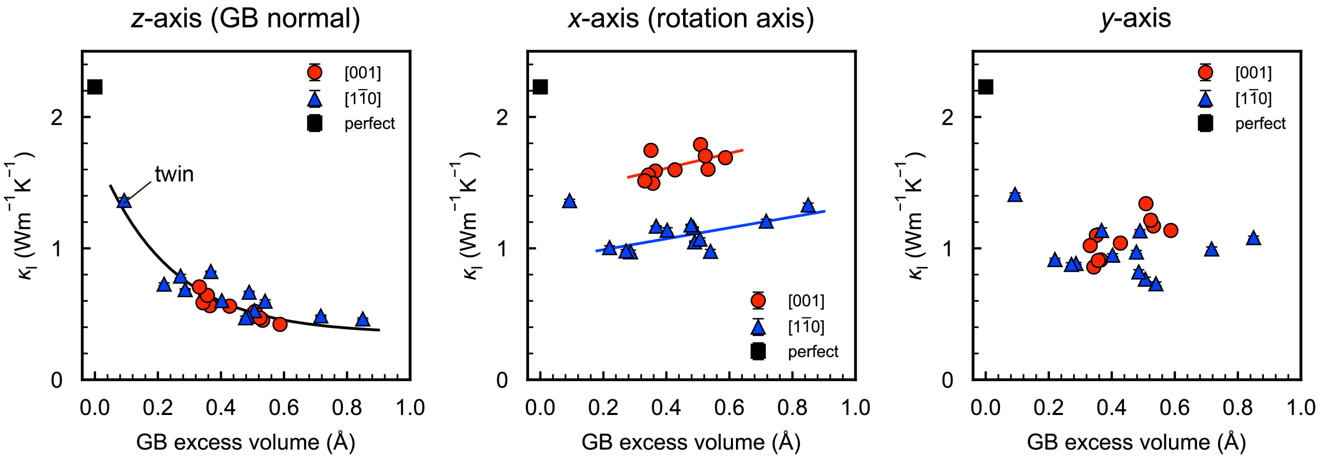

FIG. S4. Lattice thermal conductivity κ_l as a function of GB excess volume for the three axial directions. Note that the GB excess volume is evaluated from the averaged structures at 300 K.

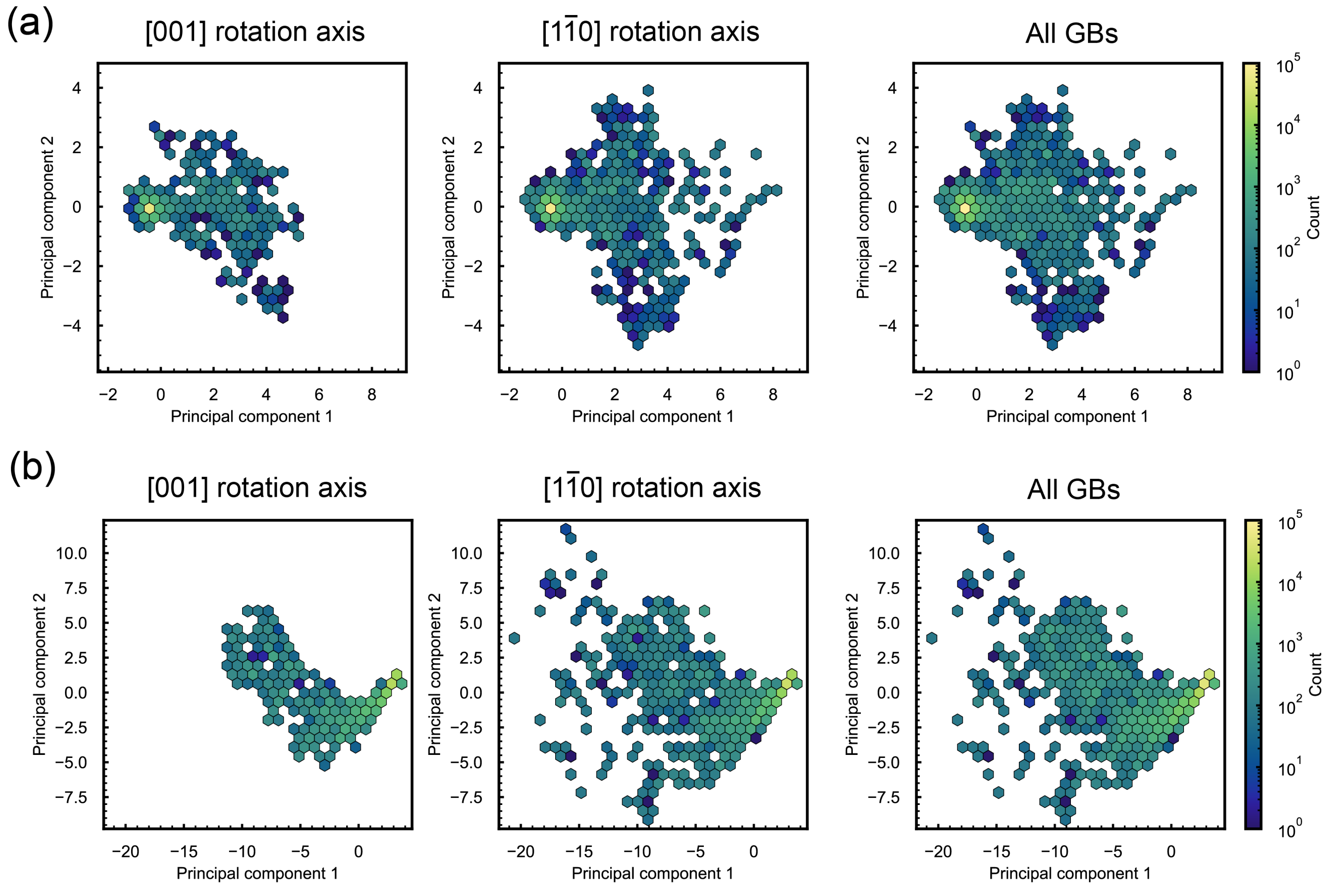

FIG. S5. Two-dimensional histogram of local atomic environments (LAEs) binned by (a) first two principal components of the SOAP vectors with a radial cutoff of 4.58 Å and (b) those with a cutoff of 25 Å. Panels show the results for the [001] system, [1$\bar{1}$0] system, and all GBs combined. Color indicates LAE counts per bin on a logarithmic scale. The cumulative explained variance ratio of the first two principal components is 0.79 for the 4.58 Å cutoff and 0.75 for the 25 Å cutoff.

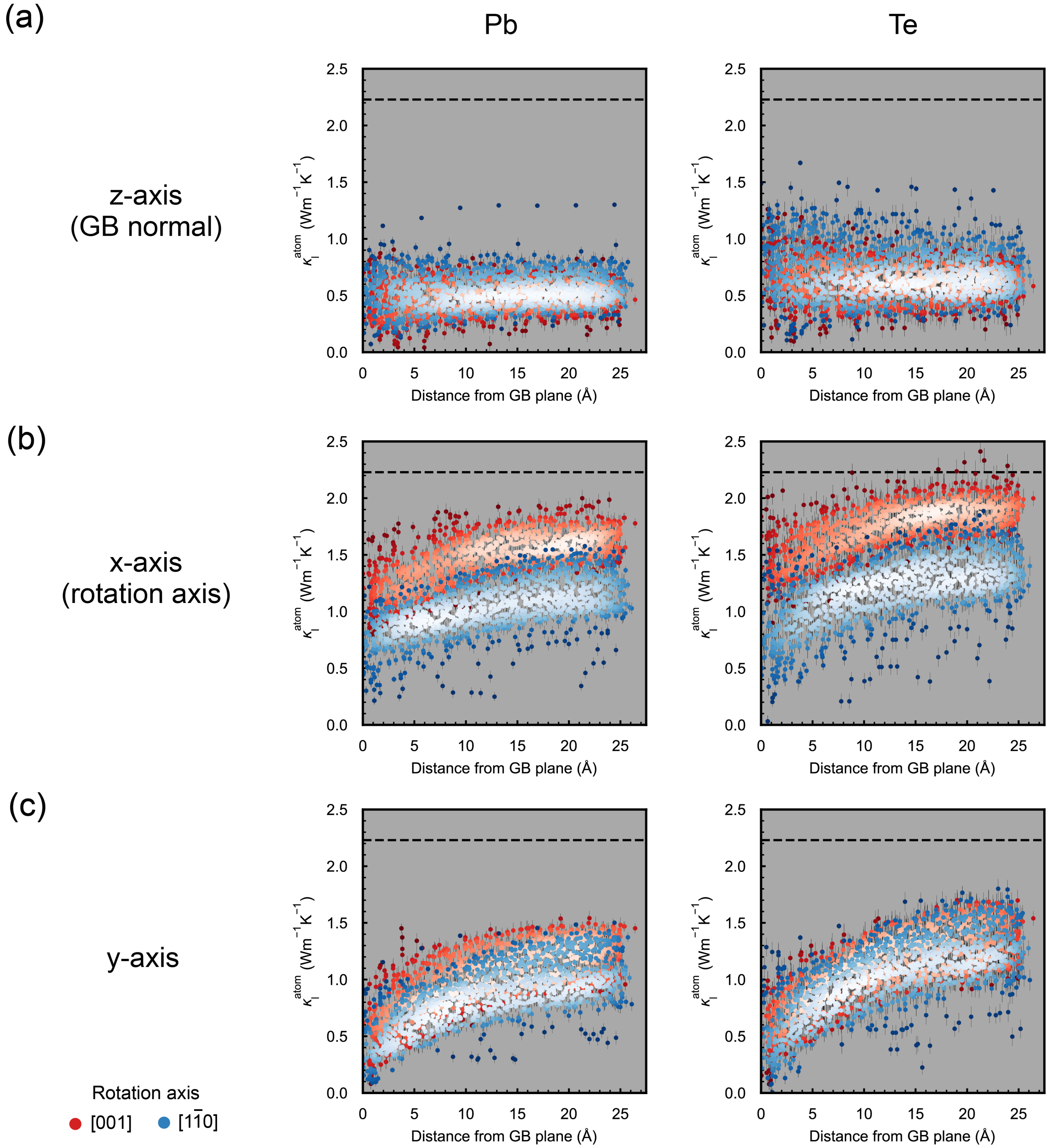

FIG. S6. Atomic thermal conductivities $\kappa_{l,i}^{\mathrm{atom}}$ of Pb and Te for all GB models as a function of the minimum distance from the two GB planes. (a) z-axis (GB normal), (b) x-axis (rotation axis), and (c) y-axis. Brighter colors indicate higher point densities.

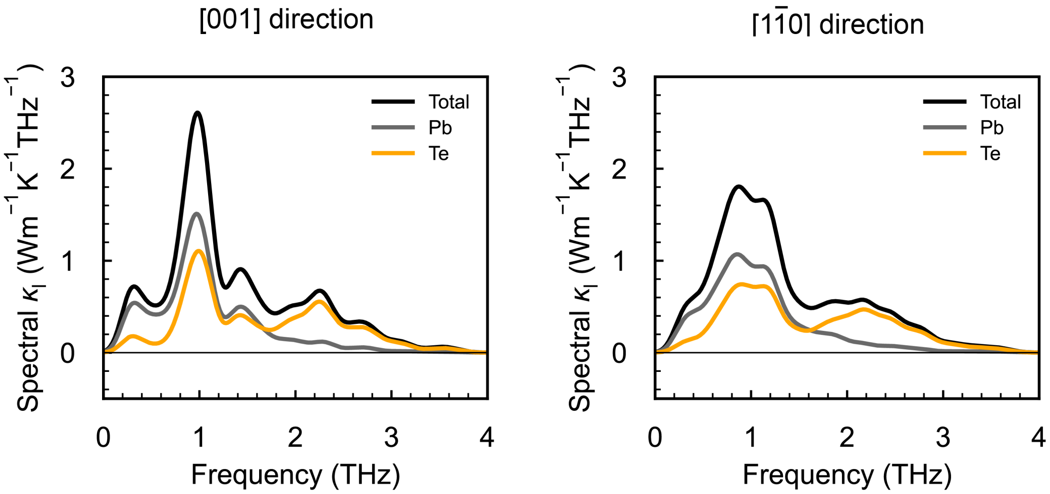

FIG. S7. Spectral κ_l along [001] and [1$\bar{1}$0] directions in the perfect crystal at 300 K. The contributions of Pb and Te on the spectral κ_l are also shown.

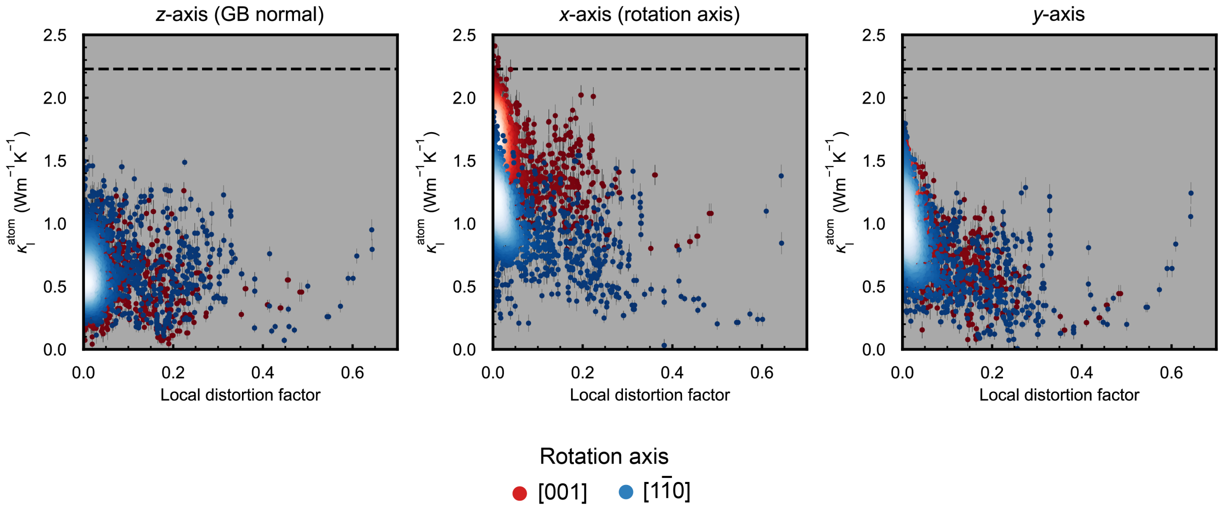

FIG. S8. Atomic thermal conductivities κ_l^{atom} for all GB models plotted against local distortion factor with a SOAP cutoff of 4.58 Å. Brighter colors indicate higher point densities.

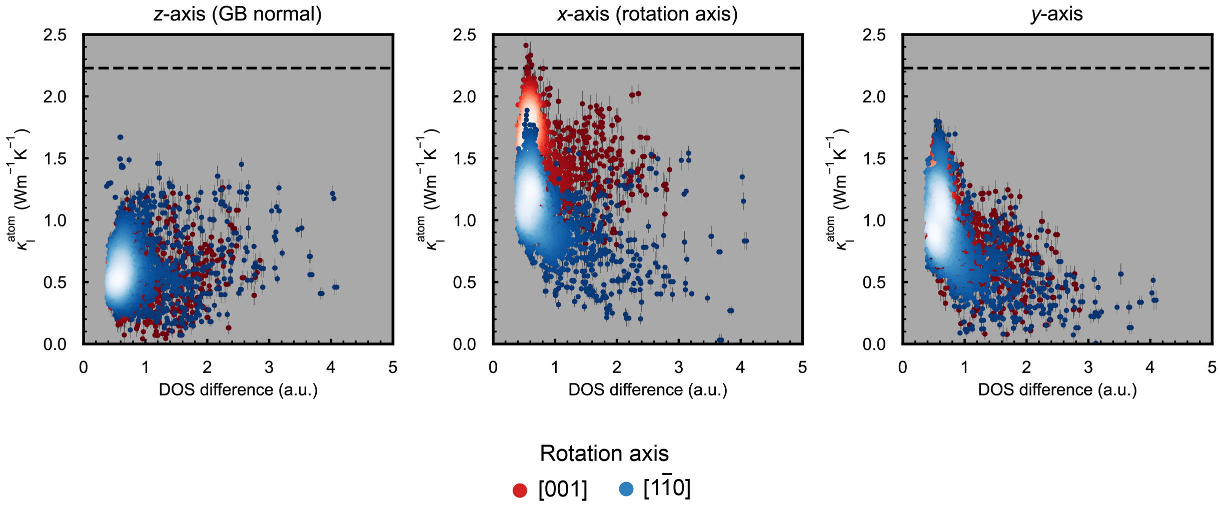

FIG. S9. Atomic thermal conductivities κ_l^{atom} for all GB models plotted against the difference in harmonic phonon density of states (DOS) between each GB atom and the corresponding bulk atom. Brighter colors indicate higher point densities.

[1] T. Yokoi, S. Fujii, Y. Ogura, and K. Matsunaga, Origin of reduced thermal conduction by native point defects in pbte: Perturbed molecular dynamics with neural network potential, Phys. Rev. B **112**, 024111 (2025).

[2] T. Yokoi, Y. Noda, A. Nakamura, and K. Matsunaga, Neural-network interatomic potential for grain boundary structures and their energetics in silicon, Phys. Rev. Mater. **4**, 014605 (2020).

[3] T. Yokoi, K. Adachi, S. Iwase, and K. Matsunaga, Accurate prediction of grain boundary structures and energetics in cdte: a machine-learning potential approach, Phys. Chem. Chem. Phys. **24**, 1620 (2022).

[4] T. Yokoi, H. Kato, Y. Oshima, and K. Matsunaga, Atomic structures of grain boundaries for si and ge: A simulated annealing method with artificial-neural-network interatomic potentials, J. Phys. Chem. Sol. **173**, 111114 (2023).

[5] A. Togo, K. Shinohara, and I. Tanaka, Spglib: a software library for crystal symmetry search, Sci. Technol. Adv. Mater., Meth. **4**, 2384822 (2024).

[6] A. Togo, L. Chaput, T. Tadano, and I. Tanaka, Implementation strategies in phonopy and phono3py, J. Phys. Condens. Matter **35**, 353001 (2023).

[7] A. Togo, First-principles phonon calculations with phonopy and phono3py, J. Phys. Soc. Jpn. **92**, 012001 (2023).